Hierarchical FeNiP @ Ultrathin Carbon Nanoflakes as Alkaline Oxygen Evolution and Acidic Hydrogen Evolution Catalyst for Efficient Water Electrolysis and Organic Decomposition

Bowei Zhang,[§] Yu Hui Lui,[§] Anand P. S. Gaur,[§] Bolin Chen,[§] Xiaohui Tang,[§] Zhiyuan Qi,[┼] and Shan Hu*[§]

[§]Department of Mechanical Engineering, Iowa State University, Ames, Iowa 50011, USA

[┼]Department of Chemistry, Iowa State University, Ames, Iowa 50011, USA

Keywords: Fe-Ni phosphide; Ultrathin carbon; OER; HER; Organic decomposition

Abstract

Efficiency of hydrogen evolution via water electrolysis is mainly impeded by the kinetically sluggish oxygen evolution reaction (OER). Thus, it is of great significance to develop highly active and stable OER catalyst for alkaline water electrolysis or to substitute the more kinetically demanding acidic OER with a facile electron-donating reaction, such that OER is no longer the bottleneck half reaction for either acidic or alkaline water electrolysis. Herein, the hierarchical Fe-Ni phosphide shelled with ultrathin carbon networks on Ni foam (FeNiP@C) is reported and shows exceptional OER activity and enhanced chemical stability in 1M KOH. This unique electrode provides large active sites, facile electron transport pathways, and rapid gas release, resulting in an remarkable OER activity that delivers a current density of 100 mA/cm^2 at an overpotential of 182 mV with a Tafel slope of 56 mV/dec. Combining the hydrogen evolution reaction (HER) with organic pollutant (methylene blue) oxidation, a multifunctional electrolyzer for simultaneous cost-effective hydrogen generation and organic pollutant decomposition in acid wastewater is proposed. Our strategies in this work provide attractive opportunities in energy and environment related fields.

1. Introduction

Electrochemical splitting of water to generate hydrogen offers an effective method to convert the renewable but intermittent sources, such as solar and wind, into energy-dense hydrogen fuels that can be stored, transported, and used upon demand.[1–5] Of the two half reactions for water splitting, the oxygen evolution reaction (OER) is the bottleneck in terms of reaction kinetics because it requires the coupled transfer of four protons and four electrons from two water molecules to generate one oxygen molecule.[6,7] To overcome the sluggish OER kinetics, efficient catalyst is in critical need. Unfortunately, most OER electrocatalysts are unstable and decayed quickly in acidic systems, even the benchmark catalysts RuO_2 and IrO_2.[8,9] This makes the alkaline water electrolyzer more popular in industrial systems. Currently, a series of transition metal-based alkaline OER catalysts with activities superior to Ru/Ir-based compounds have been reported, such as nitride,[10] phosphides,[11,12] and chalcogenides.[13] As we reported previously, Fe doped Ni_2P is an efficient OER catalyst and the $(Fe_{0.5}Ni_{0.5})_2P$/NF only needs 156 mV to deliver a 10 mA/cm^2 current density in 1M KOH.[12] The best performance was obtained in the Fe/Ni molar ratio range of about 0.1-1 and it varied slightly depending on the Fe/Ni ratio. However, the chemical stability of the transition-metal based phosphides during oxidative reactions remains an issue due to the leaching of anions.[14] To mitigate this issue, this study proposed to stabilize the catalyst-electrolyte interface with a protective coating of chemically robust nanocarbon. Additionally, the nanocarbon coating is expected to provide direct electron transport paths to the catalyst and further improve its electrocatalytic performance.[15]

For acidic water electrolysis, due to the lack of suitable OER catalyst, the alternative strategy to overcome the sluggish OER is to replace it with more facile oxidative reactions of organic substances such as ethanol, etc.[16] In this work, acidic wastewater with organic pollutants is

electrolyzed for the simultaneous hydrogen production and organic decomposition. The abundant H^+ in acidic wastewater favors the hydrogen evolution reaction, because compared to the alkaline Volmer step of reducing an adsorbed water molecule (H_2O*) into H* and OH^-, the Volmer step in acid only involves the reduction of a proton into H*.[17] Moreover, the organic pollutant is more readily oxidized than water, and hence the kinetics of anode reaction will become less of a bottleneck for the hydrogen production at the cathode. Furthermore, this "trash to treasure" design provides a more economical solution to the environmental issue aroused by organic pollutants and acidic wastewater, compared with existing complex and high-cost routes that firstly neutralize the corrosive acid wastewater by adding alkali before decomposing or separating the organic pollutants. Finally, Nickel based phosphides are well-known active and stable catalysts for hydrogen evolution reaction (HER) in acid, such as the FeNi alloy-derived Fe-P and Ni-P nanocomposite.[18] But the Fe-doped Ni phosphide solid solution for acidic HER has not been studied so far. Hence, this work will use FeNiP as the HER electrode in the multifunctional water electrolyzer/wastewater cleaner to investigate its acidic HER activity and stability.

Herein, we reported the hierarchical iron nickel phosphide shelled with amorphous carbon nanoflakes (denoted as FeNiP@C) as highly efficient and stable multifunctional catalyst for water electrolysis. The 3D ultrathin carbon networks provided a continuous pathway for facile electron transfer through the whole catalyst layer. The unique hierarchical structure of the FeNiP@C provides abundant active sites and rapid gas product release. Most importantly, the chemically robust carbon shell effectively enhanced the chemical stability of FeNiP by reducing the leaching of P element during alkaline OER. As a result, the FeNiP@C electrode shows an exceptionally high OER activity in 1M KOH and excellent HER performance in 5mM H_2SO_4. Additionally, excellent stability was observed during long-term electrolysis. Finally, using the FeNiP@C as

cathode, we prove the concept of a novel multifunctional electrolyzer for simultaneous hydrogen production and wastewater treatment by replacing the acidic OER with fast-kinetics methylene blue (MB) oxidation using the solution of 5mM H_2SO_4 + 5 mg/L MB as electrolyte. In the multifunctional cell, H^+ from the electrolyte was eliminated to produce H_2 at cathode (FeNiP@C), while MB was decomposed at the anode.

2. Material and methods

2.1 Materials and chemicals

Nickel foam (thickness: 1.6 mm, bulk density: 0.45 g/cm^3), NH_4F, urea, glucose powder, RuO_2 powder, and $NaH_2PO_2 \cdot H_2O$ were provided by Sigma Aldrich. $Ni(NO_3)_2 \cdot 6H_2O$, $Fe(NO_3)_3 \cdot 9H_2O$, KOH, and Methylene blue (MB) were purchased from Fisher Scientific. All chemicals used in this work are of analytical grade. The water used through this work was purified by Milli-Q system.

2.2 Synthesis of FeNiP and FeNiP@C

Nickel foams (NF, 2 cm × 3 cm) were carefully cleaned with the assistance of sonication in 6 M HCl, ethanol, and water for 10 min, respectively. To synthesis Fe-Ni hydroxide on nickel foam (FeNi-OH), 4 mmol of NH_4F, 10 mmol urea, 2.8 mmol $Ni(NO_3)_2 \cdot 6H_2O$, and 1.2 mmol $Fe(NO_3)_3 \cdot 9H_2O$ were dissolved in 40 mL water. Then both the solution and the prepared NF were transferred into a 50 mL Teflon autoclave, then sealed and kept at 120 °C for 9 h with a heating rate of 3 °C min^{-1}, followed by washing the product with water under the assistance of sonication and dried at 60 °C for 6 h in air. To prepare the phosphide on nickel foam, the as-synthesized FeNi-OH and 1.2 g of $NaH_2PO_2 \cdot H_2O$ were put at two ceramic boats inside a tube furnace with $NaH_2PO_2 \cdot H_2O$ powder at the upstream of the gas flow. After flushed with argon (Ar) to wash the quartz tube for a while, the center of the tube furnace was elevated to 300 °C at a ramping rate of

3 °C min^{-1} and kept at this temperature for 2 h in a static Ar atmosphere. After that, samples were naturally cooled to room temperature in the atmosphere of Ar. The distance of the two ceramic boats is about 3-5 cm. The toxic tail gas was adsorbed by a saturated $CuSO_4$ water solution. The whole tube furnace was located inside a fume hood. For the fabrication of carbon shell on the obtained FeNiP nanosheets, the sample was transferred to the Teflon autoclave with 40 mL glucose solution (0.15 M) and then maintained at 180 °C for 3-6 h in an electric oven. After cooling to room temperature, the sample was cleaned by sonication to remove the loosely attached carbon products. Finally, the sample was carbonized at 300 °C with an accelerating rate of 5 °C min^{-1} under Ar atmosphere.

2.3 Materials characterization

The crystallographic information was obtained directly form the nickel foam-based sample via X-Ray Diffraction (XRD, Siemens D500 X-ray diffractormeter) by Cu Kα radiation. The detailed morphology and structure of the materials were characterized using a FEI Titan Themis 300 Cubed probe aberration corrected scanning transmission electron microscope (STEM) and a FEI Quanta 250 field-emission scanning electron microscopy (FE-SEM). Chemical compositions and elemental oxidation states of the samples were characterized by X-ray photoelectron spectroscopy (XPS, AMICUS ESCA 3400) with Mg Kα 1253.7eV radiation. Raman spectra were recorded on LabRam HR Raman spectrometer (Horiba Jobin Yvon, France) using a wavelength of 514 nm. Inductively coupled plasma emission spectrometer (ICP-MS) was used to determine the content of various elements. Liquid Chromatography-Mass Spectrometry (LCMS, consisting of Agilent Technologies 1100 HPLC system coupled to an Agilent Technologies 6310 Ion Trap mass spectrometer) was used to detect the final products of MB decomposition.

2.4 Electrochemical measurements

All electrochemical measurements were conducted on a Gamry Interface 3000 potentiostat at room temperature in a typical three-electrode setup using electrocatalysts electrode as the working electrode, a Pt wire and a graphite rod as the counter electrodes for OER and HER tests, respectively, and Ag/AgCl and Hg/HgO electrodes as the reference electrodes. OER and HER related tests were performed in 1 M KOH and a mixed solution of 5 mM H_2SO_4 and 5 mg/L methylene blue (MB) at room temperature. Polarization curves were recorded using linear sweep voltammetry (LSV) with a scan rate of 5 mV/s and corrected by IR-compensation. All measured potentials were calibrated to RHE. Note that the mixed solution was purged by Ar before recording the polarization plots. The loading mass of FeNiP@C on NF is about 4.3 ± 0.2 mg/cm^2. RuO_2 ink was prepared by dispersing 10 mg RuO_2 powder in the mixture solution of 950 μL ethanol and 50 μL Nafion (20 wt. %). Then the as-prepared ink was coated onto nickel foam with the loading mass density of about 4.5 mg/cm^2 and dried in air at room temperature. Electrochemical impedance spectroscopy (EIS) measurements were carried out in a frequency range from 10^5 Hz to 0.1 Hz. The current density was calculated by normalizing the current with the widely used geometry area of the electrode (GA).

2.5 MB degradation and UV-Vis measurement

MB solution of commonly used concentration (5 mg/L) was used for simulating the acidic wastewater by mixing with 5 mM H_2SO_4. The absorption spectrum of the measured samples which contains MB at different times were measured by UV-vis light absorbance. 1 mL of simulated wastewater was continuously taken out from the cell at the time of 0 min, 10 min, 15 min, 20 min, 25 min, and 53 min. The obtained samples were diluted to 2 mL for more accurate UV-Vis tests.

3. Results and discussion

3.1 Fabrication and Characterization of Materials

The hierarchical structure of FeNi hydroxide (FeNi-OH) flower-like microspheres supported on FeNi-OH nanosheets layer was synthesized on Ni foam (NF, Fig. 1b) by a simple hydrothermal method at 120 ℃ for 9 h (see the experimental section for details). The time-dependent growth process was shown in Fig. S1: the flower-like sphere starts to form after 6 h but the structural collapse was observed after 12 h. We then tested the OER performances of the FeNi-OH obtained under different growth times and presented the results in Fig. S2. The 9 h-FeNi-OH exhibited the best performance and the over-grown 12 h-FeNi-OH shown lower performance than that of the 6, 7, and 9 h's samples. We therefore selected 9 h as the optimized time condition in this work. As Fig. 1a and c shows, the obtained FeNi-OH precursor was converted into porous FeNi phosphide via low-temperature phosphorization. The phase structure of the prepared FeNiP and FeNi-OH were analyzed by X-ray diffraction (XRD). The patterns in Fig. 1d are indexed well with the typical facets of FeNiP and FeNi-OH, respectively. The peaks in FeNi-OH can be assigned to typical facets of Ni-Fe hydroxide: (003), (006), (101), (012), (015), (110), and (113).[4] The peaks at 40.8°, 44.5°, 47.6°, 54.3°, 54.8° are indexed to (111), (201), (210), (300), and (211) facets of Ni-P facets (PDF#04-004-5163).[11] The three major peaks at 44.7°, 52°, and 76.5° are corresponding to the metallic Ni in the nickel foam substrate. Note that all the peaks are shifted due to the incorporation of Fe. After phosphorization, a carbon layer was coated on the hierarchical FeNiP via hydrothermal carbonization of glucose. During the hydrothermal process, glucose molecules were first cross-linked by dehydration process to form a network that wraps the entire hierarchical FeNiP structure and then cross-linked organic network was turned into a carbonized layer with abundant oxygen functional groups. The sample was further carbonized at 300 ℃ for 2 h under argon atmosphere

and the final product was named as FeNiP@C (Fe/Ni/P molar ratio ~ 3/7/5, determined by ICP-MS). We can see from the detailed SEM images in Fig. 1e-g that the FeNiP@C surface become rugged due to the integration of carbon networks to the FeNiP nanosheets. This hierarchical carbon shell provides facile electron transfer pathways between the active catalyst and the current collector (Fig. 1a). As shown in Fig. 1g, the hierarchical porous structure also provides reactant/product exchange channels between neighboring chambers that are constructed by porous FeNiP@C nanosheet arrays. High-angle-annular-dark-field scanning transmission electron microscopy (HAADF-STEM) was employed to further study the FeNiP@C. It confirms the porous nature of the FeNiP@C nanosheets (Fig. 2a). The thicknesses of the carbon nanoflake and the carbon shell surrounding the FeNiP nanosheets can be observed from Fig. 2b and 2e, both of which are about 4 nm. Energy dispersive X-ray (EDX) mapping in Fig. 2c demonstrates the homogeneous distribution of Ni, Fe, P, and C. Note that the denser carbon spots in area 1 (Fig. 2c) compared with that in area 2 and the corresponding higher carbon EDX intensity in area 1 (Fig. 2d) was aroused by the carbon coating on the STEM copper grid. In Fig. 2e, carbon nanoflakes were clearly observed and the Fast Fourier transformation (FFT) indicates its amorphous nature. The denoted lattice spacing of 0.22 nm in Fig. 2f can be indexed to the (111) crystal plane of FeNiP.[19] Some FeNiP crystalline clusters were trapped in the amorphous carbon shell (as shown in Fig. S3), which might contribute significantly to the catalysis activity.[20]

Fig. S4 shows the X-ray photoelectron spectroscopy (XPS) spectra for FeNiP@C. The survey spectrum confirms the coexistence of Fe, Ni, P, and C elements. The spectrum in the Ni 2p region (Fig. S4b) shows a doublet at 856.5 and 874.3 eV (Ni^{2+}) with two shakeup satellites.[4,21] The Fe 2p spectrum (Fig. S4c) is fitted with three peaks (at 707.6, 712, and 724.5 eV) assigned to Fe^{2+} and a peak at 716.2 eV assigned to Fe^{3+}.[4] Note that no peak characteristic of Fe_2P was observed in the

Fe 2p region, indicating the formation of a ternary compound rather than a mixture of Fe_2P and Ni_2P solid phases.[22] In Fig. S4d, the P 2p spectrum shows two peaks at 130.2 and 133.9 eV reflecting the binding energies of phosphide and oxidized P species arising from superficial oxidation of the phosphide exposed in air.[12] Because XPS is a surface sensitive technique probing a depth of only a few nanometers from the surface, it is reasonably to deduce that the carbon layer coated on FeNiP is ultrathin because the P $2p_{1/2}$ (130.2 eV) peak can still be detected even if it is weak. In the high-resolution spectrum of C 1s (Fig. S4e), the bonding energies at 282.7, 284.6 and 288.5 eV should be assigned to sp^2-hybridized carbon atoms (−C−C−), C=C, and C(O)O, respectively.[23,24] According to the previous analysis, the peak at 531.2 and 533.3 eV in O 1s (Fig. S4f) can be assigned to the hydroxide group and C−O−C, respectively. To some degree, the bonding energy at 531.2 eV could be assigned to -COOH. We believe that this observation indicates the successful coating of oxygen-functionalized carbon on FeNiP.

To further investigate the nature of the hierarchical carbon layer, Raman spectrum of FeNiP@C was recorded at ambient temperature using the excitation wavelength of 514 nm (Fig. S5). The spectrum was fitted into four bands by Gaussian Function, which centers at 1180 (sp^3 rich phase), 1373 (D band), 1490 (aromatic oligomers), and 1596 cm^{-1} (G band), respectively. As the physical properties of amorphous carbon are primarily determined by the ratio of sp^2 and sp^3 bonded carbon, Raman probe is frequently used to approximate this fraction by measuring the band position, width, and intensity ratio of D and G bands (I_D/I_G).[25] Robertson *et.al.* has proposed a model based on G band position and I_D/I_G ratio (ratio of fitted peak area) to elaborate the shape of Raman spectrum in order to identify the nature of amorphous carbon, nano-crystalline graphite, and diamond-like carbon (sp^3) rich phase.[26] In this work, the G band position was found to be ~1600 cm^{-1} and the calculated I_D/I_G ratio is 0.96 (~ 1). Hence, the sp^2 bonded hierarchical carbon coating

on FeNiP rendered facile conductive channel for electrons and further contributed to improve the electrochemical performance.

3.2. Electrochemical Evaluation of FeNiP@C for OER in Alkaline Condition

To investigate the role of the ultrathin amorphous carbon on the catalytic activity of the FeNiP@C electrode, a series of electrochemical tests were carried out in 1M KOH using the typical three-electrode system. In Fig. 3a, the OER polarization curve of FeNiP@C and FeNiP show much better activity than RuO_2. Compared with FeNiP electrode, the FeNiP@C shows significantly enhanced OER performance due to the existence of ultrathin carbon coating on its surface. To deliver a current density of 100 mA/cm^2, the FeNiP@C only needs an extremely low overpotential of 182 mV (Fig. 3b) with the smallest Tafel slope of 56 mV/dec (Fig. 3c). As the comparison Table S1 shows, the excellent performance of FeNiP@C is among the best in the recently reported most-active alkaline OER electrocatalysts, including NiFe-OH/NiFeP/NF (η_{300mA/cm^2} = 258 mV, 39 mV/dec),[22] Co/Co_2P/NF (η_{50mA/cm^2} = 190 mV, 59.8 mV/dec),[27] $Fe(PO_3)_2/Ni_2P$ /NF (η_{10mA/cm^2} = 177 mV, 51.9 mV/dec),[28] MnO_2-CoP_3 (η_{10mA/cm^2} = 288 mV, 59 mV/dec),[29] and FeNiP/NF (η_{20mA/cm^2} = 219 mV, 57 mV/dec).[30] The OER process recorded in Movie S1 shows the good gas desorption ability of the FeNiP@C electrode.

To further clarify the role of the ultrathin carbon shell on the greatly enhanced OER performance, we measured and analyzed the electrochemical active surface area (ECSA) and electrochemical impedance spectroscopy. To compare the ECSA, double-layer capacitance (C_{dl}) was measured using cyclic voltammetry (CV) method in a non-Faradaic region at various scan rates (Fig. S6 shows the details).[11] As shown in Fig. 3d, the ECSA of FeNiP@C (5.65 mF/cm^2) is higher than that of FeNiP electrode (4.4 mF/cm^2), indicating a ~ 28% increase attributed to the carbon layer. We extended the time of hydrothermal process of glucose to 6 h and studied the

product (FeNiP@C-2) as well. SEM images in Fig. S7a and b show the carbon nanoflakes become denser and the overall thickness of the carbon layer increased, compared with the FeNiP@C with 3h hydrothermal carbonization. The significantly decreased ECSA of FeNiP@C-2 (1.8 mF/cm^2) in Fig. S7c and d indicates the overgrown carbon layer blocks the accessible active sites for electrochemical reactions. Moreover, electrochemical impedance spectroscopy (EIS) tests were conducted to study the reaction kinetics during OER, as shown in Fig. 3e. The intercept of the Nyquist plot of FeNiP@C with the real axis is slightly smaller than that of FeNiP, indicating lower electrode resistance and/or lower interfacial resistance between FeNiP@C and electrolyte. It is more important to note that the FeNiP@C shows a much smaller semicircle in the low-frequency region compared with FeNiP electrode, indicating smaller charge transfer resistance or faster kinetics during OER.

Durability of catalyst is a major concern for water oxidation, thus a long-term operation at 100 mA/cm^2 was employed to evaluate the durability of FeNiP@C (Fig. 3f). There is no significant increase of measured potential, indicating the good stability of FeNiP@C. Its structural stability was confirmed by SEM after the long-term stability test (Fig. S8). The observed stability could be partially attributed to the unique electrode structure, which provided a good gas release ability and avoided the structure collapse aroused by the gas accumulation. As previously reported that the P element in the outer layer of phosphide will leach into the electrolyte. Hence, it is necessary to investigate the P leaching of FeNiP@C in this work. After the stability tests at the same current density of 100 mA/cm^2 for 2h, the surface chemical composition of the post-OER FeNiP@C and FeNiP samples were analyzed by XPS, respectively (Fig. S9). Note that the carbon layer would not affect the Fe/Ni ratio in FeNiP. From the sensitive XPS data, the intensity of P detected from post-OER FeNiP is negligible compared with that of FeNiP@C and post-OER FeNiP@C.

Additionally, we conducted the stability tests for FeNiP and FeNiP@C with a same geometry area (~ 2 cm^2) at a constant current density of 100 mA/cm^2 in 40 mL KOH electrolyte for 10 h, respectively. Then the concentrations of Fe, Ni, and P in the obtained two electrolytes were determined by ICP-MS. Table S2 shows that no Fe and Ni were detected from the two electrolytes, confirming there is no detectable Fe or Ni leaching for both FeNiP and FeNiP@C. Interestingly, the P concentration in the electrolyte of FeNiP@C (10.799 ppm) is only about 10% of the corresponding electrolyte of FeNiP electrode (106.113 ppm), as the inset table in Fig. 3f shows. We also characterized the FeNiP@C electrode before and after the electrochemical OER test by XRD and XPS. As shown in Fig. S10, the typical peaks of Ni_2P seems slightly weaker than the pure FeNiP in Figure 1d due to the existence of amorphous carbon shell and there is no significant difference between the two XRD patterns, indicating the major phase of the active catalyst is FeNiP. Therefore, these results indicate that the carbon layer effectively reduced the leaching of P in FeNiP, which suggests carbon coating is a promising strategy for improving the chemical stability of electrodes that are involved in interfacial electrochemical oxidation reactions, for applications such as the electrocatalysis and pseudocapacitor, etc. High resolution XPS spectra for P 2p obtained from FeNiP@C before and after the electrochemical OER test are compared in Figure S11. Based on the XPS, the P content in the post-OER FeNiP@C is 33.2 % of that in the pre-OER FeNiP@C, demonstrating the P leaching occurred. However, it should be noted that XPS is mostly sensitive to surface composition of the sample. Hence, the XPS results do not provide the P content within the bulk FeNiP@C. In fact, we have previously found that during OER, P was mainly leached from the surface thin layer of the FeNiP.[12]

3.3. Acidic Water Electrolysis by Substituting OER with Organic Oxidation

Acid system is beneficial to HER, but its application is hindered by the sluggish OER half reaction and the lack of suitable non-precious-metal OER catalysts. To overcome this challenge, we designed an unconventional acidic water electrolyzer (Fig. 4a), in which the electron donating half reaction was no longer the OER but the oxidative decomposition of organic pollutant, methylene blue (MB). In the proposed electrolyzer, the anode is the low-cost graphite rod, the cathode is FeNiP@C, and the electrolyte is synthetic wastewater (5 mM H_2SO_4 + 0~100 mg/L MB). As we previously mentioned that the acid OER is very sluggish and corrosive and the metal-based compounds cannot resist the acidic oxidative condition, but the carbon materials have better stability.[31] This is the reason why we choose the low-cost graphite rod as the anode. It is important to note that the nickel foam was widely used in the acid system (0.5 M H_2SO_4) and exhibited good stability. The OER onset potential in pure H_2SO_4 is about 1.8 V (Fig. 4b), which is comparable the reported acid OER performance.[6,9] The onset potential was calculated according to the previous report by W. Schuhmann, et al.[32] In the presence of MB, a lower onset potential ascribed to the oxidation of MB was observed from ~1.2 V. Thus, MB oxidation dominates a wide potential range of ~ 1.2 V to ~ 1.8 V. Significant current increases were observed in both the MB oxidation dominant and OER dominant ranges following the increase of MB concertation from 5 to 100 mg/L, indicating MB oxidation has fast kinetics. Therefore, MB oxidation reaction is a good candidate to substitute acidic OER and further makes the hydrogen generation in acidic condition more practical.

The electrocatalytic HER activity and stability of FeNiP@C were evaluated in a solution of 5 mM H_2SO_4 + 5 mg/L MB (pH~2, close to real wastewater) using a standard three-electrode configuration with graphite rod as the counter electrode. 5 mg/L is a typical concentration of artificial wastewater in lab.[33–36] LSV curves in Fig. 4c shows that the FeNiP@C needs the lowest

overpotential of 104 mV to afford the current density of -10 mA/cm^2 with the Tafel slope of 54.6 mV/dec. The HER performance of FeNiP@C is comparable to the best non-noble metal HER catalysts even if their performances were recorded in more acidic electrolyte of 0.5 M H_2SO_4, e.g., $NiSe_2$/NF (η_{10mA/cm^2} = 143 mV),[37] porous Co-based film/Au film (η_{10mA/cm^2} = 150 mV),[38] FeCoP (η_{10mA/cm^2} = 37 mV),[39] $NiCo_2P_x$ (η_{10mA/cm^2} = 104 mV),[40] and np-$(Co_{0.52}Fe_{0.48})_2P$ (η_{10mA/cm^2} = 64 mV).[41] It is important to note that the HER process has higher kinetics in 0.5 M H_2SO_4 than 5 mM H_2SO_4 due to the higher H^+ in it. The Nyquist plots of FeNiP@C and FeNiP electrodes have been measured at – 0.1 V vs RHE as well (Fig. S12). FeNiP@C electrode shows an enhanced charger transfer ability during HER process compared to FeNiP, which can be ascribed to the ultrathin carbon shell. As for the stability of FeNiP@C, no significant decay was observed after 1000 cycles of CV scans between 0.2 and -0.2 V vs. RHE at a scan rate of 100 mV/s, as shown in Fig. 4d. Movie S2 in the supporting information shows the process of hydrogen generation at FeNiP@C, but no oxygen bubble generated on the anode surface, indicating no OER happens at the graphite rod counter electrode. After 500 CV cycles between - 0.2 V ~ 0 V vs RHE, we tested the P content of the electrolyte by ICP-MS as well. A 17 ppm P element was found in the post-HER electrolyte (~ 23 mL), indicating there is a P leaching during the HER process. Similar phenomena of P leaching have been reported during alkaline HER process.[42]

The continuous degradation process of MB by the proposed acidic water electrolyzer functioning at a current density of 1 mA/cm^2 was monitored by UV-Vis absorption study. At different degradation time, the electrolyte sample was collected from the electrolyzer and the absorption spectrum of the sample was measured with UV-Vis spectrophotometer. Following the increase of degradation time, the absorbance peak at ~ 650 nm becomes weaker (Fig. 4e), indicating the disappearance of the MB. The MB degradation process can also be observed from

the corresponding color change of the electrolyte as shown in the inset of Fig. 4e. After 53 min, the MB in the electrolyte was completely decomposed. During this process under a constant current density of 1 mA/cm^2, the corresponding potential (~1.72 V) is stable (Fig. 4f). It has been reported previously that the final decomposition product of MB during photocatalysis process is CO_2 and H_2O,[35,36] but the final products of MB are still need to be investigated during electrocatalysis process. To identify the final products of MB for this study, LCMS (Liquid Chromatography-Mass Spectrometry) was used. As shown in Fig. S13, the peak of MB at time 12.8 min became invisible after the decomposition compared with the profile of the original MB solution. A new peak appeared after decomposition at 1 min with a peak area that is much smaller than that of MB (Fig. S13b). As the MB decomposition is a complex multi-step process that produces many intermediate organic products,[43,44] we ascribe the new peak to the residual intermediate organic products, which are yet to be further decomposed and have much lower concentration than the original MB. Thus, we conclude that MB has been almost completely decomposed by the electrocatalysis process and most of the final decomposition products should be inorganics, which might be CO_2 and H_2O.

4. Conclusion

In this study, we demonstrated the conductive carbon networks coated hierarchical FeNi phosphide (FeNiP@C) can serve as an exceptionally efficient alkaline OER and acidic HER electrocatalyst. The highly active FeNiP@C electrode was fabricated by cost-effective hydrothermal, annealing, and carbonization processes. The hierarchical porous structure of FeNiP provided large surface area and interconnected channels for mass transport and gas release. The conductive carbon coating led to facile transport of electrons throughout the entire electrode. Moreover, the carbon coating played a key role in reducing the leaching of P in FeNiP and provided

an efficient way for improving chemical stability of the widely reported transition-metal based nitrides, sulfides, selenides, and phosphide. By substituting the OER process with fast-kinetics oxidative reaction of organic pollutant in a synthetic wastewater, the energy-saving hydrogen generation and wastewater cleaning were achieved simultaneously. We believe that our work not only provides a strategy for developing exceptionally efficient and more chemically stable electrode for various electrochemical applications but also proposes a new solution in producing hydrogen from acidic system and in organic pollutant decomposition.

ASSOCIATED CONTENTS

Supporting Information

The Supporting Information is available free of charge on the ACS Publications website at DOI:

Description of sample preparation, materials characterization, electrochemical tests, UV-Vis test, supplementary SEM images, electrochemical data and analysis, LCMS tests, and ICP-MS results.

AUTHOR INFORMATION

*Corresponding to: shanhu@iastate.edu

ACKNOWLEDGEMANTS

This material is based upon work supported by the National Science Foundation under Grant No. CMMI-1663509 and the startup funding from Department of Mechanical Engineering, Iowa State University (ISU). B. Z. was supported by the Catron Fellowship from the College of Engineering, ISU. HAADF-STEM and EDX characterizations were carried out in Ames National Lab, US Department of Energy. All the SEM, XRD, XPS characterizations were done in The Materials Analysis and Research Laboratory (MARL) of the ISU Office of Biotechnology. The authors thank the W.M. Keck Metabolomics Research Laboratory at ISU for the assistance on LCMS tests.

Notes

The author declare no financial interest conflict.

References

(1) Long, X.; Wang, Z.; Xiao, S.; An, Y.; Yang, S. Transition Metal Based Layered Double Hydroxides Tailored for Energy Conversion and Storage. *Mater. Today* **2016**, *19* (4), 213–226.

(2) Xu, S.; Chen, Y.; Li, Y.; Lu, A.; Yao, Y.; Dai, J.; Wang, Y.; Liu, B.; Lacey, S. D.; Pastel, G. R.; Kuang, Y.; Danner, V. A.; Jiang, F.; Fu, K. K.; Hu, L. Universal, in Situ Transformation of Bulky Compounds into Nanoscale Catalysts by High-Temperature Pulse. *Nano Lett.* **2017**, *17* (9), 5817–5822.

(3) Peng, X.; Hu, L.; Wang, L.; Zhang, X.; Fu, J.; Huo, K.; Lee, L. Y. S.; Wong, K. Y.; Chu, P. K. Vanadium Carbide Nanoparticles Encapsulated in Graphitic Carbon Network Nanosheets: A High-Efficiency Electrocatalyst for Hydrogen Evolution Reaction. *Nano Energy* **2016**, *26*, 603–609.

(4) Zhang, B.; Hu, S. Turning Ni-Based Hydroxide into an Efficient Hydrogen Evolution Electrocatalyst by Fluoride Incorporation. *Electrochem. commun.* **2018**, *86* (November 2017), 108–112.

(5) Zhao, G.; Sun, Y.; Zhou, W.; Wang, X.; Chang, K.; Liu, G.; Liu, H.; Kako, T.; Ye, J. Superior Photocatalytic H2Production with Cocatalytic Co/Ni Species Anchored on Sulfide Semiconductor. *Adv. Mater.* **2017**, *29* (40), 1–9.

(6) Huynh, M.; Bediako, D. K.; Nocera, D. G. A Functionally Stable Manganese Oxide Oxygen Evolution Catalyst in Acid. *J. Am. Chem. Soc.* **2014**, *136* (16), 6002–6010.

(7) Peng, X.; Wang, L.; Hu, L.; Li, Y.; Gao, B.; Song, H.; Huang, C.; Zhang, X.; Fu, J.; Huo,

K.; Chu, P. K. In Situ Segregation of Cobalt Nanoparticles on VN Nanosheets via Nitriding of Co2V2O7nanosheets as Efficient Oxygen Evolution Reaction Electrocatalysts. *Nano Energy* **2017**, *34* (February), 1–7.

(8) Frydendal, R.; Paoli, E. A.; Chorkendorff, I.; Rossmeisl, J.; Stephens, I. E. L. Toward an Active and Stable Catalyst for Oxygen Evolution in Acidic Media: Ti-Stabilized MnO2. *Adv. Energy Mater.* **2015**, *5* (22).

(9) Moreno-Hernandez, I. A.; MacFarland, C. A.; Read, C. G.; Brunschwig, B. S.; Papadantonakis, K. M.; Lewis, N. Crystalline Nickel Manganese Antimonate as a Stable Water-Oxidation Catalyst in Aqueous 1.0 M H_2SO_4. *Energy Environ. Sci.* **2017**, *10*, 2103–2108.

(10) Zhang, Y.; Ouyang, B.; Xu, J.; Jia, G.; Chen, S.; Rawat, R. S.; Fan, H. J. Rapid Synthesis of Cobalt Nitride Nanowires: Highly Efficient and Low-Cost Catalysts for Oxygen Evolution. *Angew. Chemie - Int. Ed.* **2016**, *55* (30), 8670–8674.

(11) Zhang, B.; Lui, Y. H.; Zhou, L.; Tang, X.; Hu, S. An Alkaline Electro-Activated Fe–Ni Phosphide Nanoparticle-Stack Array for High-Performance Oxygen Evolution under Alkaline and Neutral Conditions. *J. Mater. Chem. A* **2017**, *5* (26), 13329–13335.

(12) Zhang, B.; Lui, Y. H.; Ni, H.; Hu, S. Bimetallic (FexNi1−x)2P Nanoarrays as Exceptionally Efficient Electrocatalysts for Oxygen Evolution in Alkaline and Neutral Media. *Nano Energy* **2017**, *38* (June), 553–560.

(13) Wang, Z.; Li, J.; Tian, X.; Wang, X.; Yu, Y.; Owusu, K. A.; He, L.; Mai, L. Porous Nickel-Iron Selenide Nanosheets as Highly Efficient Electrocatalysts for Oxygen Evolution

Reaction. *ACS Appl. Mater. Interfaces* **2016**, *8* (30), 19386–19392.

(14) Wang, X.; Li, W.; Xiong, D.; Liu, L. Fast Fabrication of Self-Supported Porous Nickel Phosphide Foam for Efficient, Durable Oxygen Evolution and Overall Water Splitting. *J. Mater. Chem. A* **2016**, *4* (15), 5639–5646.

(15) Bae, S. H.; Kim, J. E.; Randriamahazaka, H.; Moon, S. Y.; Park, J. Y.; Oh, I. K. Seamlessly Conductive 3D Nanoarchitecture of Core–Shell Ni-Co Nanowire Network for Highly Efficient Oxygen Evolution. *Adv. Energy Mater.* **2017**, *7* (1), 1–11.

(16) You, B.; Liu, X.; Jiang, N.; Sun, Y. A General Strategy for Decoupled Hydrogen Production from Water Splitting by Integrating Oxidative Biomass Valorization. *J. Am. Chem. Soc.* **2016**, *138* (41), 13639–13646.

(17) Gong, M.; Wang, D. Y.; Chen, C. C.; Hwang, B. J.; Dai, H. A Mini Review on Nickel-Based Electrocatalysts for Alkaline Hydrogen Evolution Reaction. *Nano Res.* **2016**, *9* (1), 28–46.

(18) Read, C. G.; Callejas, J. F.; Holder, C. F.; Schaak, R. E. General Strategy for the Synthesis of Transition Metal Phosphide Films for Electrocatalytic Hydrogen and Oxygen Evolution. *ACS Appl. Mater. Interfaces* **2016**, *8* (20), 12798–12803.

(19) Li, P.; Zeng, H. C. Advanced Oxygen Evolution Catalysis by Bimetallic Ni–Fe Phosphide Nanoparticles Encapsulated in Nitrogen, Phosphorus, and Sulphur Tri-Doped Porous Carbon. *Chem. Commun.* **2017**, *53* (44), 6025–6028.

(20) Tang, C.; Wang, H. Sen; Wang, H. F.; Zhang, Q.; Tian, G. L.; Nie, J. Q.; Wei, F. Spatially

Confined Hybridization of Nanometer-Sized NiFe Hydroxides into Nitrogen-Doped Graphene Frameworks Leading to Superior Oxygen Evolution Reactivity. *Adv. Mater.* **2015**, *27* (30), 4516–4522.

(21) Zhang, B.; Ni, H.; Chen, R.; Zhan, W.; Zhang, C.; Lei, R.; Zha, Y. A Two-Step Anodic Method to Fabricate Self-Organised Nanopore Arrays on Stainless Steel. *Appl. Surf. Sci.* **2015**, *351*, 1161–1168.

(22) Liang, H.; Gandi, A. N.; Xia, C.; Hedhili, M. N.; Anjum, D. H.; Schwingenschlögl, U.; Alshareef, H. N. Amorphous NiFe-OH/NiFeP Electrocatalyst Fabricated at Low Temperature for Water Oxidation Applications. *ACS Energy Lett.* **2017**, *2* (5), 1035–1042.

(23) Wang, G.; Wang, H.; Lu, X.; Ling, Y.; Yu, M.; Zhai, T.; Tong, Y.; Li, Y. Solid-State Supercapacitor Based on Activated Carbon Cloths Exhibits Excellent Rate Capability. *Adv. Mater.* **2014**, *26* (17), 2676–2682.

(24) Zhang, B.; Ni, H.; Chen, R.; Zhang, T.; Li, X.; Zhan, W.; Wang, Z.; Xu, Y. Cytotoxicity Effects of Three-Dimensional Graphene in NIH-3T3 Fibroblasts. *RSC Adv.* **2016**, *6* (51), 45093–45102.

(25) Wang, Z.; Ni, H.; Chen, R.; Zhan, W.; Zhang, C.; Lei, R.; Zhang, B. Enhanced Performance of Multilayer Graphene Platelet Film via Three Dimensional Configuration with Efficient Exposure of Graphitic Edge Planes. *Electrochem. commun.* **2014**, *47*, 75–79.

(26) Ferrari, A. C.; Robertson, J. Resonant Raman Spectroscopy of Disordered, Amorphous, and Diamondlike Carbon. *Phys. Rev. B - Condens. Matter Mater. Phys.* **2001**, *64* (7), 1–13.

(27) Masa, J.; Barwe, S.; Andronescu, C.; Sinev, I.; Ruff, A.; Jayaramulu, K.; Elumeeva, K.; Konkena, B.; Roldan Cuenya, B.; Schuhmann, W. Low Overpotential Water Splitting Using Cobalt–Cobalt Phosphide Nanoparticles Supported on Nickel Foam. *ACS Energy Lett.* **2016**, *1* (6), 1192–1198.

(28) Zhou, H.; Yu, F.; Sun, J.; He, R.; Chen, S.; Chu, C.-W.; Ren, Z. Highly Active Catalyst Derived from a 3D Foam of $Fe(PO_3)_2/Ni_2P$ for Extremely Efficient Water Oxidation. *Proc. Natl. Acad. Sci.* **2017**, *114* (22), 5607–5611.

(29) Xiong, X.; Ji, Y.; Xie, M.; You, C.; Yang, L.; Liu, Z.; Asiri, A. M.; Sun, X. MnO2-CoP3nanowires Array: An Efficient Electrocatalyst for Alkaline Oxygen Evolution Reaction with Enhanced Activity. *Electrochem. commun.* **2018**, *86* (November 2017), 161–165.

(30) Yu, J.; Cheng, G.; Luo, W. Hierarchical NiFeP Microflowers Directly Grown on Ni Foam for Efficient Electrocatalytic Oxygen Evolution. *J. Mater. Chem. A* **2017**, *5* (22), 11229–11235.

(31) Yang, X.; Li, H.; Lu, A. Y.; Min, S.; Idriss, Z.; Hedhili, M. N.; Huang, K. W.; Idriss, H.; Li, L. J. Highly Acid-Durable Carbon Coated Co3O4nanoarrays as Efficient Oxygen Evolution Electrocatalysts. *Nano Energy* **2016**, *25*, 42–50.

(32) Botz, A. J. R.; Nebel, M.; Rincón, R. A.; Ventosa, E.; Schuhmann, W. Onset Potential Determination at Gas-Evolving Catalysts by Means of Constant-Distance Mode Positioning of Nanoelectrodes. *Electrochim. Acta* **2015**, *179*, 38–44.

(33) Lei, R.; Ni, H.; Chen, R.; Gu, H.; Zhang, B.; Zhan, W. Hydrothermal Synthesis of CdS

Nanorods Anchored on α-Fe2O3 Nanotube Arrays with Enhanced Visible-Light-Driven Photocatalytic Properties. *J. Colloid Interface Sci.* **2018**, *514*.

(34) Lei, R.; Ni, H.; Chen, R.; Zhang, B.; Zhan, W.; Li, Y. Hydrothermal Synthesis of WO3/ Fe2O3 Nanosheet Arrays on Iron Foil for Photocatalytic Degradation of Methylene Blue. *J Mater Sci Mater Electron* **2017**, *28*, 10481–10487.

(35) Xue, X.; Zang, W.; Deng, P.; Wang, Q.; Xing, L.; Zhang, Y.; Wang, Z. L. Piezo-Potential Enhanced Photocatalytic Degradation of Organic Dye Using ZnO Nanowires. *Nano Energy* **2015**, *13*, 414–422.

(36) Lei, R.; Ni, H.; Chen, R.; Zhang, B.; Zhan, W.; Li, Y. Growth of Fe2O3/SnO2 Nanobelt Arrays on Iron Foil for Efficient Photocatalytic Degradation of Methylene Blue. *Chem. Phys. Lett.* **2017**, *673*, 1–6.

(37) Zhou, H.; Wang, Y.; He, R.; Yu, F.; Sun, J.; Wang, F.; Lan, Y.; Ren, Z.; Chen, S. One-Step Synthesis of Self-Supported Porous NiSe2/Ni Hybrid Foam: An Efficient 3D Electrode for Hydrogen Evolution Reaction. *Nano Energy* **2016**, *20*, 29–36.

(38) Yang, Y.; Fei, H.; Ruan, G.; Tour, J. M. Porous Cobalt-Based Thin Film as a Bifunctional Catalyst for Hydrogen Generation and Oxygen Generation. *Adv. Mater.* **2015**, *27* (20), 3175–3180.

(39) Tang, C.; Gan, L.; Zhang, R.; Lu, W.; Jiang, X.; Asiri, A. M.; Sun, X.; Wang, J.; Chen, L. Ternary FexCo1-xP Nanowire Array as a Robust Hydrogen Evolution Reaction Electrocatalyst with Pt-like Activity: Experimental and Theoretical Insight. *Nano Lett.* **2016**, *16* (10), 6617–6621.

(40) Zhang, R.; Wang, X.; Yu, S.; Wen, T.; Zhu, X.; Yang, F.; Sun, X.; Wang, X.; Hu, W. Ternary $NiCo_2P_x$ Nanowires as pH-Universal Electrocatalysts for Highly Efficient Hydrogen Evolution Reaction. *Adv. Mater.* **2017**, *29* (9), 1605502.

(41) Tan, Y.; Wang, H.; Liu, P.; Shen, Y.; Cheng, C.; Hirata, A.; Fujita, T.; Tang, Z.; Chen, M. Versatile Nanoporous Bimetallic Phosphides towards Electrochemical Water Splitting. *Energy Environ. Sci.* **2016**, *9* (7), 2257–2261.

(42) Wang, X.; Li, W.; Xiong, D.; Petrovykh, D. Y.; Liu, L. Bifunctional Nickel Phosphide Nanocatalysts Supported on Carbon Fiber Paper for Highly Efficient and Stable Overall Water Splitting. *Adv. Funct. Mater.* **2016**, *26* (23), 4067–4077.

(43) Rauf, M. A.; Meetani, M. A.; Khaleel, A.; Ahmed, A. Photocatalytic Degradation of Methylene Blue Using a Mixed Catalyst and Product Analysis by LC/MS. *Chem. Eng. J.* **2010**, *157* (2–3), 373–378.

(44) Ray, S. K.; Dhakal, D.; Kshetri, Y. K.; Lee, S. W. Cu-α-NiMoO4photocatalyst for Degradation of Methylene Blue with Pathways and Antibacterial Performance. *J. Photochem. Photobiol. A Chem.* **2017**, *348*, 18–32.

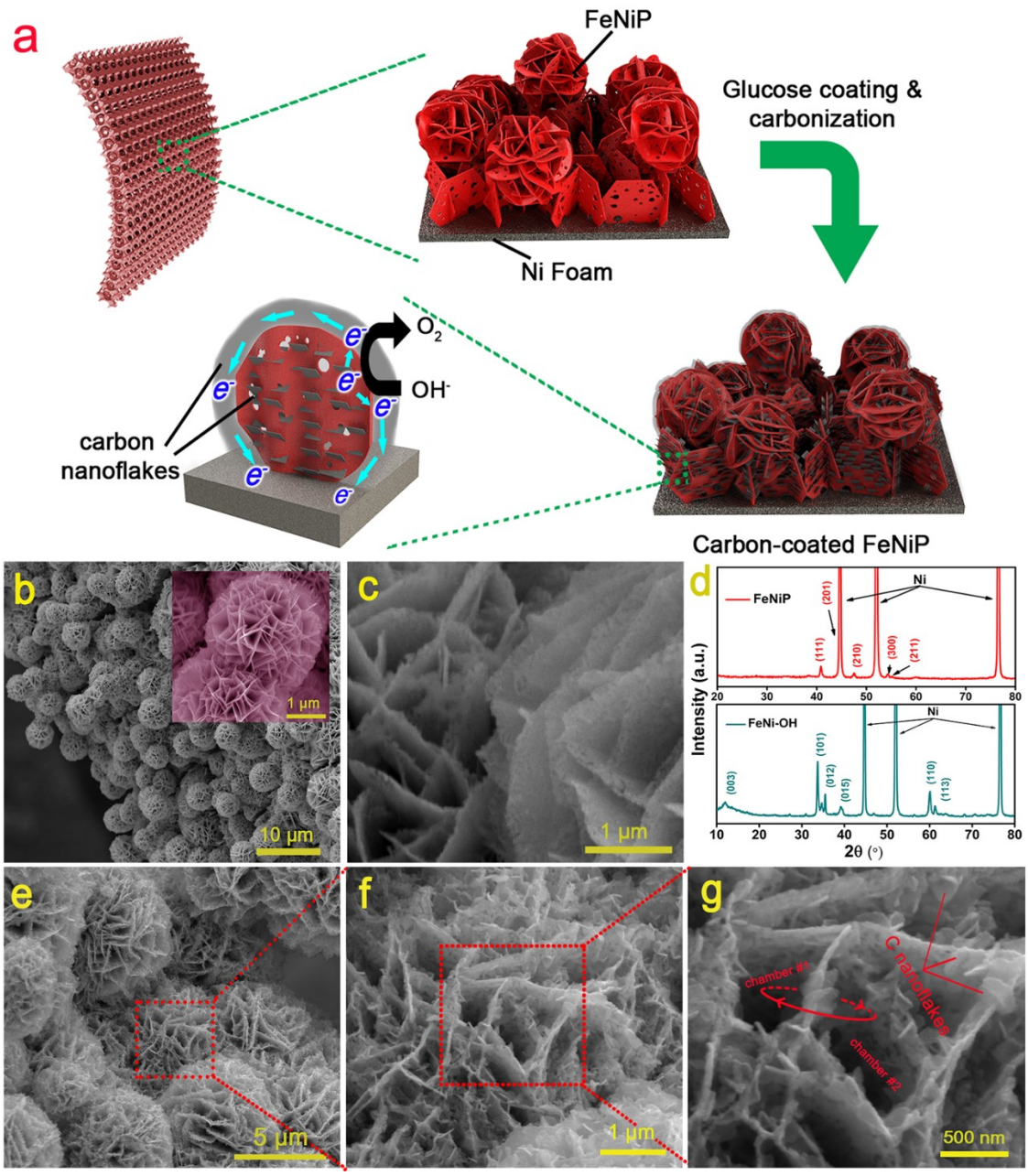

Fig. 1. (a) Schematic illustration of the fabrication route of the hierarchical FeNiP@C electrode and the facile channels for electron transfer. SEM images of (b) FeNi hydroxide precursor with micro-flower spheres supported on FeNi-OH nanosheet arrays layer that integrated on Ni foam and (c) FeNi-OH derived porous FeNi phosphide (FeNiP). (d) XRD patterns of FeNiP and FeNi-OH. (e-g) High-resolution SEM images of hierarchical FeNiP with ultrathin carbon nanoflakes coating.

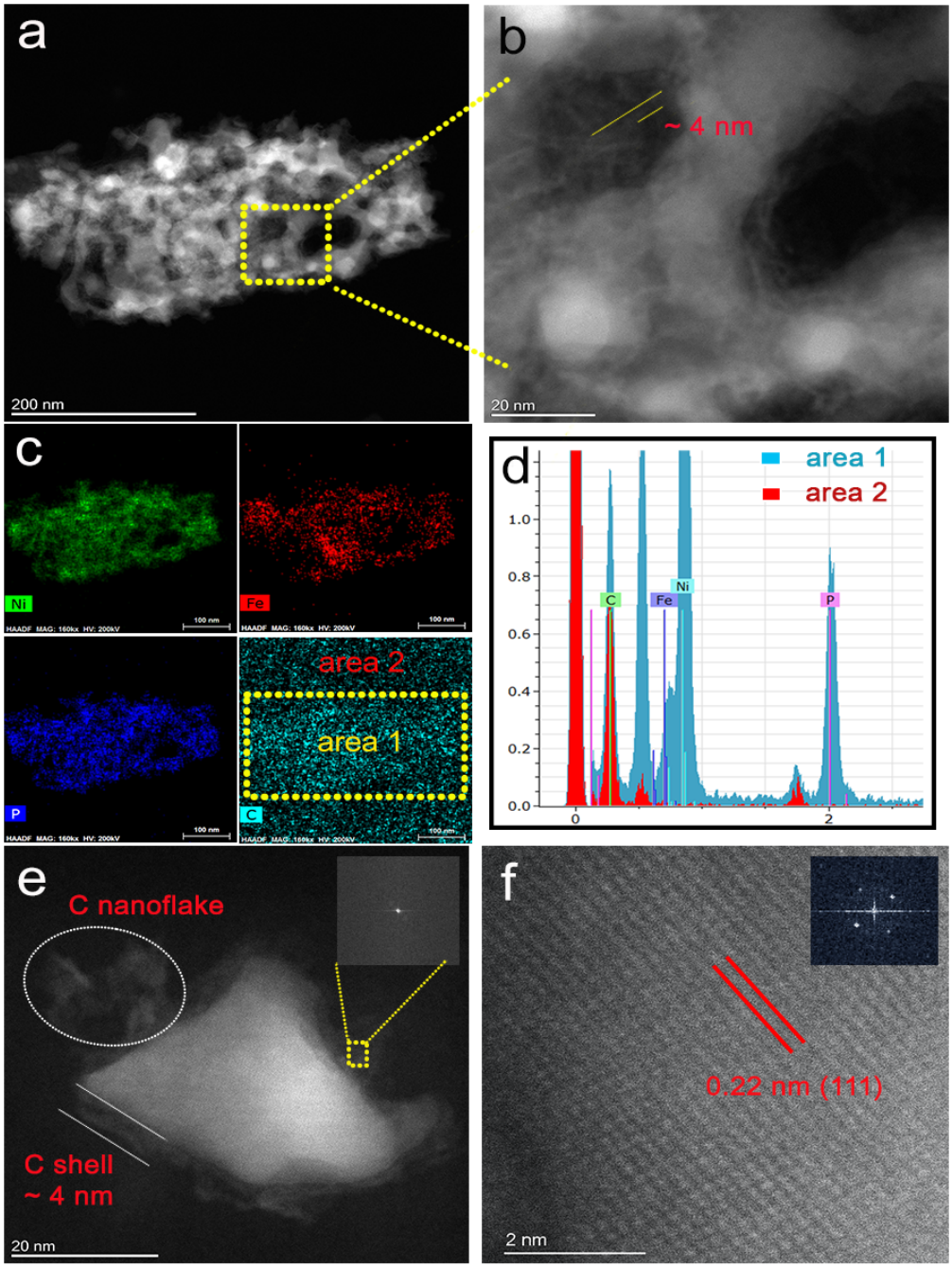

Fig. 2. (a-b) HAADF-STEM images and (c) EDX mapping of various elements for porous FeNiP@C nanosheets. The spots in area 2 of carbon mapping was aroused by the carbon coating on the grid. (d) EDX intensity comparison on area 1 (FeNiP) and area 2 (STEM grid). (e-f) High-resolution HAADF-STEM image of FeNiP@C fragment and the corresponding FFT patterns for carbon (inset in e) and FeNiP (inset in (f), respectively.

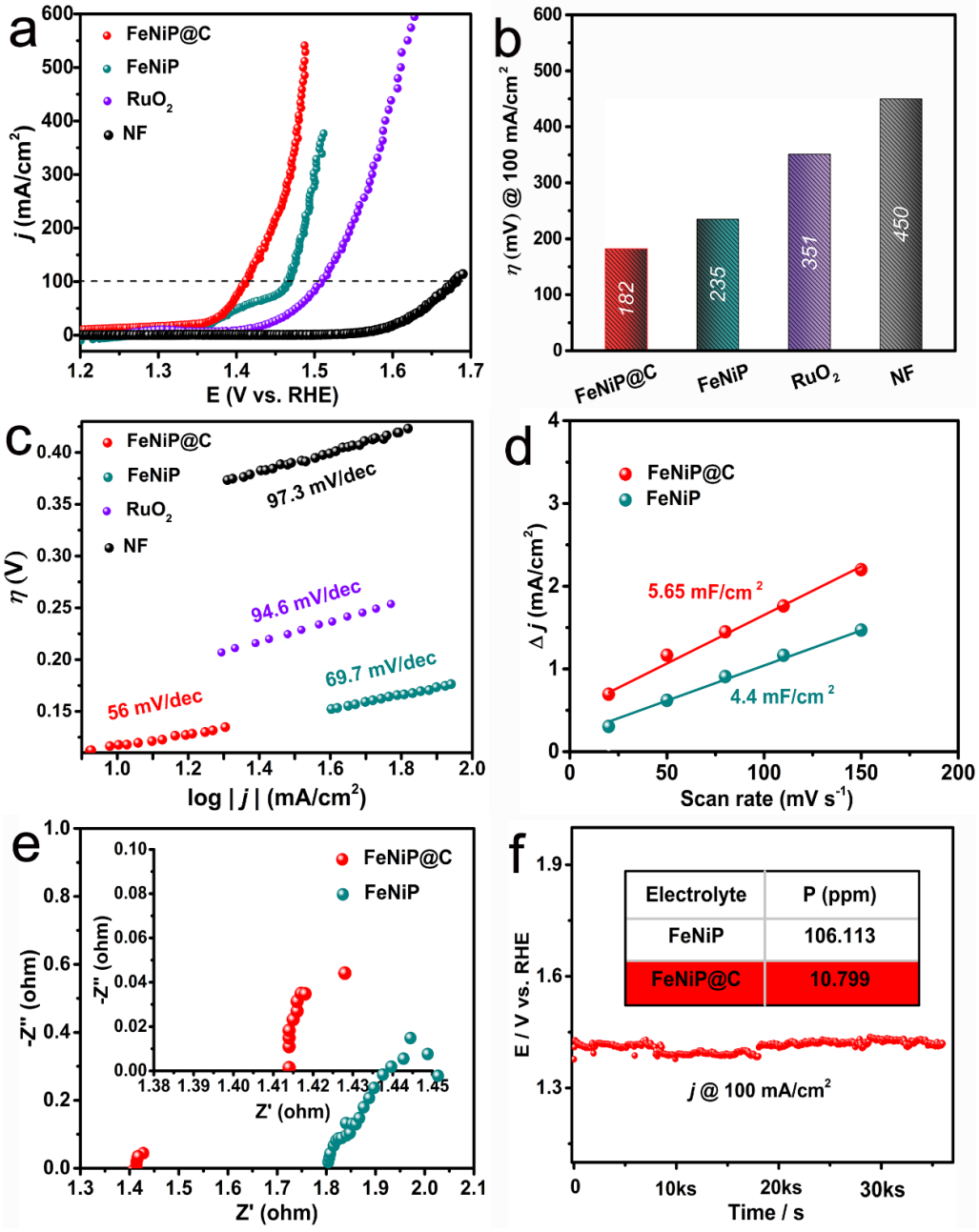

Fig. 3. Evaluations of FeNiP@C electrode for OER in 1M KOH. (a) OER Polarization curves and (b) overpotentials at the current density of 100 mA/cm^2 of various electrodes. (c) The corresponding Tafel slopes. (d) Comparison of electrochemical active surface areas (ECSA) of FeNiP and FeNiP@C electrodes. (e) Nyquist plots of different electrodes at 1.55 V vs. RHE. (f) Long-term test of FeNiP@C electrode for OER. Inset table in (f) shows the concentrations of P in the post-OER electrolytes of FeNiP and FeNiP@C electrodes.

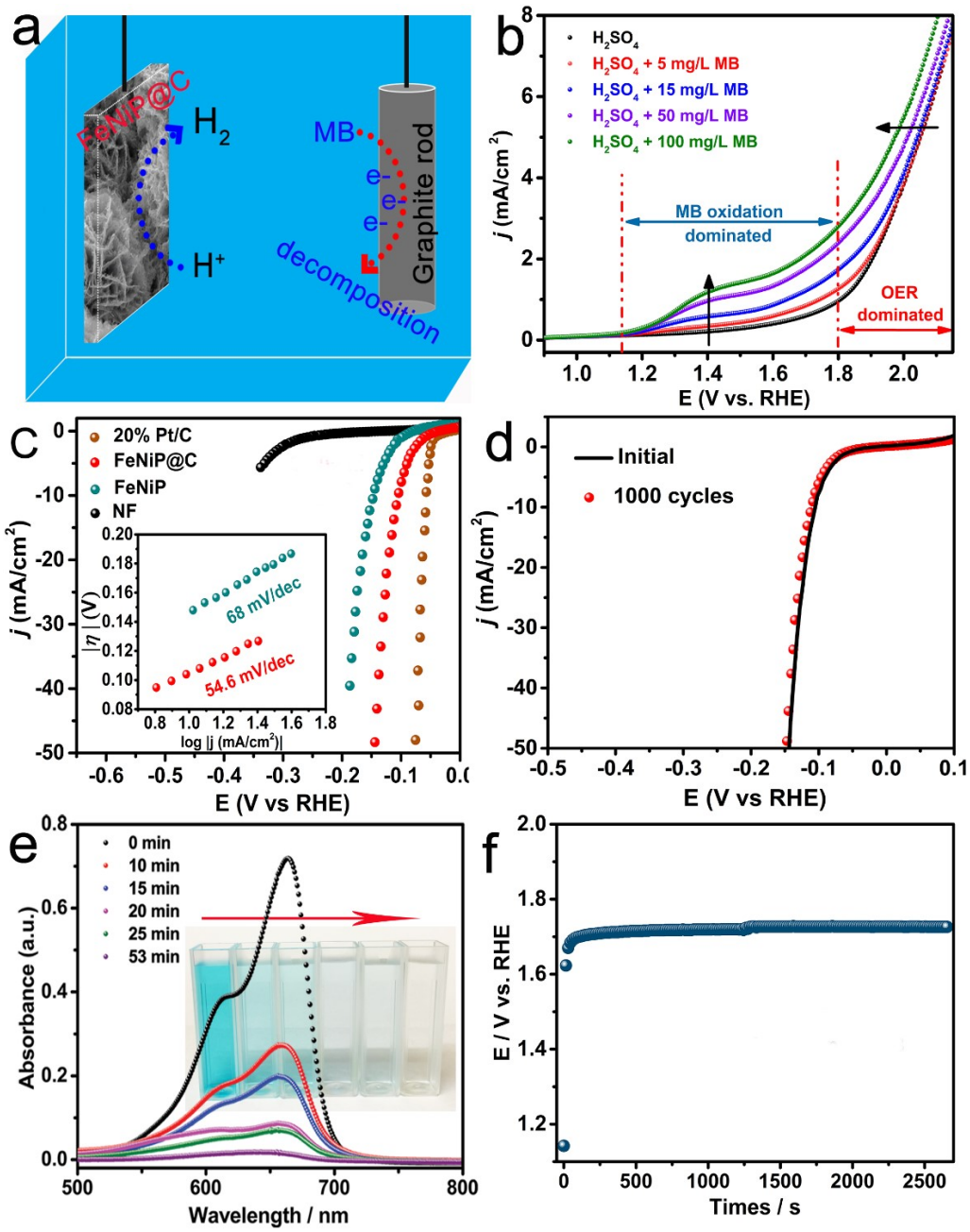

Fig. 4. (a) Illustrations of the HER and organic dye oxidation in the synthetic acidic wastewater: acidic components from wastewater offer H^+ for H_2 production at cathode, while MB is decomposed as anodic substitution for OER. (b) The polarization curves at anode in 5 mM H_2SO_4 with gradient concentrations of MB (without using *iR*-corrections). (c) HER polarization curves of various electrodes in the mixed solution of 5 mM H_2SO_4 and 5 mg/L MB. (d) LSV curves of FeNiP@C before and after 1000 CV cycles. (e) UV-Vis adsorption spectrum of MB in the mixed solution after different degradation times: 0-53 mins. Inset shows the corresponding continuous color changes process. (f) Anodic MB decomposition current density with the corresponding time-dependent potential.

Graphic Abstract